energies

MDPI

Article

Experimental Study on Overvoltage Propagation Characteristics of High-Voltage Submarine Cables

Youcong Huang [1,2], Wenqi Li [1], Junfeng Zhang [1,*], Tongtong He [3] and Yuesheng Zheng [3]

[1] State Grid Fujian Electric Power Research Institute, Fuzhou 350000, China; hyoucong@163.com (Y.H.); lwq8304@163.com (W.L.)
[2] Department of Electrical Engineering, Tsinghua University, Beijing 100084, China
[3] College of Electrical Engineering and Automation, Fuzhou University, Fuzhou 350108, China; hett@fzu.edu.cn (T.H.); yueshengzheng@fzu.edu.cn (Y.Z.)
* Correspondence: 15638293798@163.com

Abstract

With the large-scale development of deep-sea offshore wind power, the insulation safety of high-voltage submarine cable outer sheaths faces severe challenges, yet the propagation characteristics and coupling mechanisms of cable-core overvoltages to the metal sheath remain unclear. To address this, a physical experimental platform was established for lightning impulse testing based on a 66 kV submarine cable, and the transient potential response characteristics of the metal sheath under various operating conditions were systematically investigated. The results indicate that under fully suspended conditions, the sheath voltage is primarily determined by the voltage division caused by the radial coaxial distributed capacitance. When a 30.6 kV lightning impulse voltage is applied, the overall potential of the sheath approaches that of the cable core; under conditions where the sheath is grounded at the end, the capacitively coupled charge is rapidly discharged, and the transient potential is then dominated by inductive coupling, with its variation strictly corresponding to the rate of change in the cable-core's transient current; under conditions where the sheath is fully suspended and the cable core is grounded, the potential of the metal sheath exhibits a dynamic superposition of the radial capacitive common-mode voltage and the axial inductive differential-mode potential difference. These findings demonstrate that metallic-sheath grounding conditions significantly influence the relative contributions of capacitive and inductive coupling to transient sheath overvoltages under lightning impulse excitation. The experimental results provide a physical basis for further investigation of sheath grounding arrangements and overvoltage protection strategies.

Keywords: submarine cables; overvoltage propagation; capacitive coupling; inductive coupling

Check for updates

Academic Editor: Wenjun Ning

Received: 17 September 2026
Revised: 28 October 2026
Accepted: 29 October 2026
Published: 2 November 2026

Copyright: © 2026 by the authors. Licensee MDPI, Basel, Switzerland. This article is an open access article distributed under the terms and conditions of the Creative Commons Attribution (CC BY) license.

1. Introduction

As the global energy structure accelerates its transition toward clean, low-carbon sources, wind power—a renewable energy source characterized by mature technology and strong economic viability—has become a core driver of the global energy transformation [1,2]. Compared to onshore wind power, offshore wind power offers significant advantages, including stable wind resources, high annual utilization hours, and no occupation of land resources [3], and has entered a phase of rapid development worldwide in recent years [4]. According to data from the Global Wind Energy Council, by the end of 2025, the global cumulative installed capacity of offshore wind power had reached 92.5 GW,

poised to surpass the 100 GW milestone [5]. Among these, China's offshore wind power industry has shown particularly strong growth momentum [6–10], with cumulative installed capacity reaching 52 GW by the end of 2025. Offshore wind power is gradually transitioning from a supplementary and alternative energy source to a primary energy source [11–14].

Submarine cables are core components of offshore wind power transmission systems, playing a crucial role in efficiently transmitting wind energy from offshore wind farms to onshore load centers [15]. They offer technical advantages such as high transmission capacity, low line losses, and minimal susceptibility to environmental interference. However, submarine cables typically employ a solid-insulation structure [16], and insulation breakdown is irreversible [17]. Once a fault occurs, it directly triggers a forced shutdown of the transmission system and may even trigger large-scale disconnection of wind turbines from the grid, resulting in major power outages and economic losses amounting to hundreds of millions of dollars [18]. As offshore wind power expands into deeper waters, submarine cable voltage levels continue to rise, and line lengths continue to increase, significantly intensifying the system's capacitive rise effect [19] and thereby rendering the threat of transient overvoltages increasingly severe [20–22]. Ensuring the insulation safety of submarine cables has thus become a core issue constraining the reliable operation of offshore wind power projects.

From the perspective of submarine cable insulation systems, the main insulation layer on the outer side of the cable core typically has a high design margin, and the risk of breakdown during normal operation and under most transient conditions is relatively low [23,24]. In contrast, the insulation structure of the outer sheath, located on the exterior of the metal sheath, is relatively weak and is a high-risk area for insulation failures in submarine cables [25,26]. Practical operational experience has shown that flexible DC submarine cable lines have experienced multiple failures of the Sheath Voltage Limiter caused by transient overvoltage surges.

Scholars have conducted extensive research both domestically and internationally on overvoltages in submarine cables, with the focus primarily on cable simulation modeling, system-level overvoltage characteristic analysis, and insulation configuration optimization. For example, P. Thararak et al. used the PSCAD/EMTDC electromagnetic transient simulation tool to establish a model of a 115 kV hybrid submarine–land cable system and conducted a comparative analysis of the distribution patterns of switching overvoltages and the suppression effectiveness of surge arresters [27]. Roberto Benato et al., using the 380 kV AC interconnection project in southern Italy as a case study, employed EMTP-RV simulation software to establish a system model incorporating submarine and terrestrial cables [28]. VAIDEKI S et al. used ANSYS Maxwell (14.0) electromagnetic field simulation software to investigate the internal electric field distribution characteristics of high-voltage direct-current submarine cables under different insulation materials [29].

With regard to induced voltages in the metal sheaths of cables, existing research has primarily focused on terrestrial cables, while findings related to submarine cables are relatively scarce. Although the capacitive coupling method, commonly used in engineering, is computationally simple and widely applied, it is derived based on the assumption of a semi-infinite submarine cable. Consequently, its calculation results tend to be conservative and fail to accurately reflect the effects of factors such as the waveform of the incident wave, line length, and laying method on the induced voltage in the sheath [30].

In offshore wind power systems, lightning strikes on wind turbines, offshore substations, or connected overhead lines may generate steep-front overvoltages that propagate to the submarine cable terminations. Rapid voltage and current changes caused by such surges can induce transient voltages on the metal sheath through capacitive and inductive coupling, thereby potentially threatening the sheath insulation and related protective de-

vices. Therefore, this paper employs a standard 1.2/50 μs lightning impulse to investigate the coupling mechanisms by which overvoltages propagate from the cable conductor to the metal sheath under different grounding conditions, providing an experimental basis for understanding transient voltage stresses on the metal sheath and improving overvoltage protection strategies.

2. Experimental Platform and Experimental Protocol

To investigate the propagation mechanism of overvoltage in the submarine cable core, this study established a lightning impulse test platform. The overall wiring diagram is shown in Figure 1.

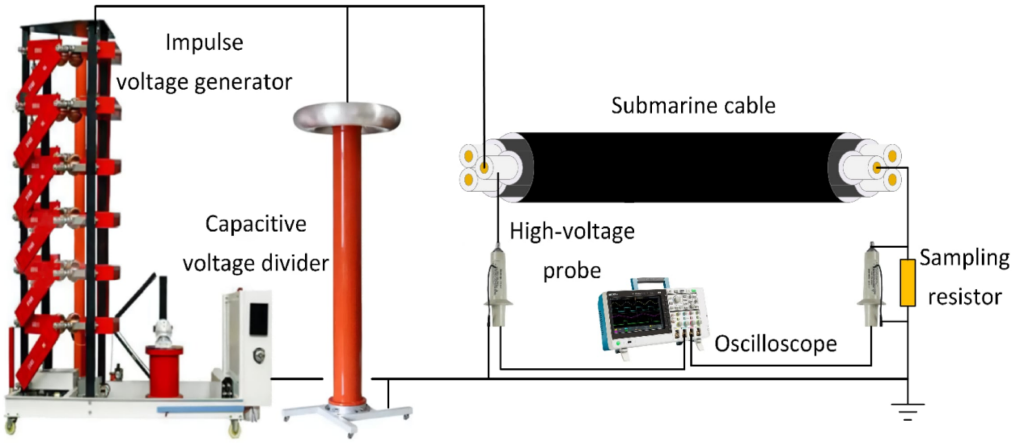


Figure 1. Schematic diagram of the lightning-impulse test platform for submarine-cable overvoltage coupling experiments.

The core equipment of the platform is a lightning impulse voltage generator, which is primarily used for full-wave lightning impulse voltage testing of electrical equipment. A weakly damped capacitive voltage divider is connected in parallel across the output terminals of the impulse voltage generator to monitor the actual lightning surge voltage applied. It serves as a standard voltage measurement device to calibrate the output voltage amplitude and monitor the waveform. The output of the low-voltage arm of the capacitive voltage divider is connected to an oscilloscope, and the high-voltage arm and low-voltage arm together provide a voltage division ratio of 1000:1, meeting the measurement requirements for high-amplitude impulse voltages. During the test, both the surge voltage generator and the capacitive voltage divider are reliably grounded.

The high-voltage output terminal of the impulse voltage generator was connected to the cable core of the submarine cable. The submarine cable was laid horizontally on insulated supports, with the metal sheath maintained at a distance of no less than 50 cm from the ground to minimize the influence of stray capacitance parameters. Before the experiment, a short section of the cable core and metal sheath at both ends of the submarine cable was stripped to facilitate equipment wiring.

The submarine cable specimen was 7 m long, with a rated voltage of 38/66 kV and a model designation of HYJQF41-F38/66-3×95+OFC+2×48B1.3. It is a three-core optical-fiber composite submarine cable with water-blocked copper conductors, XLPE insulation, separate lead sheaths, and steel-wire armor. Each power conductor has a nominal cross-sectional area of 95 mm^2, and the cable incorporates two optical-fiber units, each containing 48 B1.3 single-mode fibers. The nominal XLPE insulation thickness is approximately 14 mm. The cross-sectional structure of the cable is illustrated in Figure 2, and its principal structural parameters are summarized in Table 1.

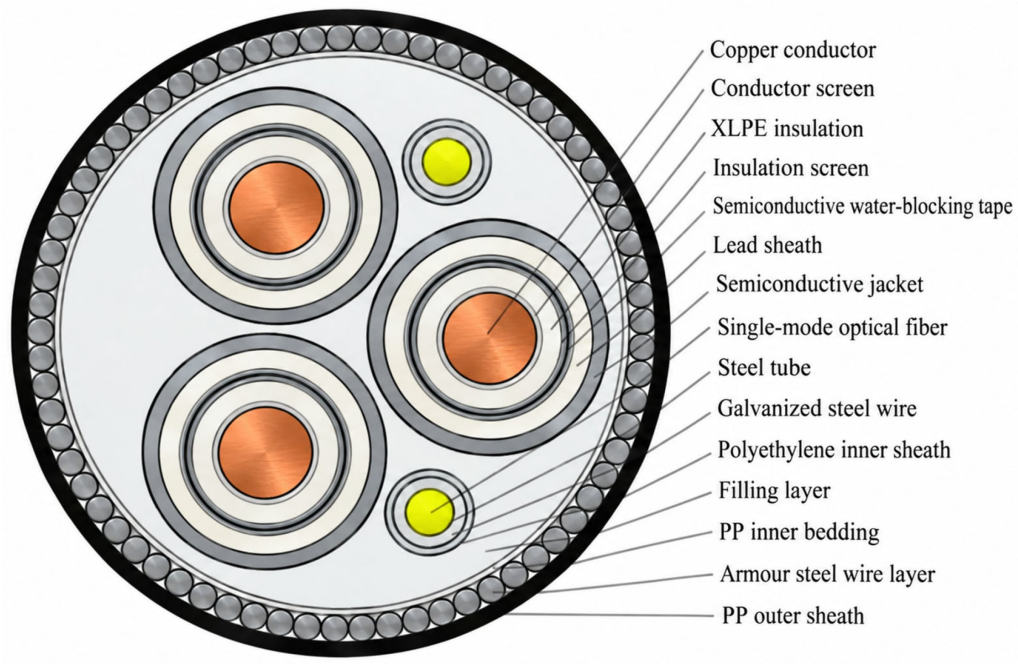


Figure 2. Cross-sectional view of submarine cable structure.

Table 1. Structural parameters of the submarine cable.

Parameter	Value
Conductor material	Water-blocked copper
Nominal conductor cross-sectional area	95 mm^2 per core
conductor diameter	12.12 mm
XLPE insulation thickness	14 mm
outer diameter of conductor screen, XLPE insulation, and insulation screen assembly	43.07 mm
outer diameter of semiconductive water-blocking layer	43.63 mm
outer diameter of lead sheath	48.28 mm
outer diameter of PE sheath	51.66 mm
lead sheath thickness	2.32 mm
Estimated lead sheath cross-sectional area	335.5 mm^2
Overall cable diameter	133.69 mm
Optical fiber configuration	2 × 48 B1.3 single-mode fibers

To accurately capture voltage signals from the cable core and metal sheath of a submarine cable, this study configured a high-voltage probe connected to an oscilloscope to enable simultaneous acquisition of voltage waveforms. To minimize electromagnetic interference during the lightning impulse tests, the impulse voltage generator and the low-voltage measuring instruments were physically separated by approximately 10 m. The oscilloscope was supplied through an isolation transformer equipped with a grounded electrostatic shield between its primary and secondary windings to reduce interference coupled through the power supply. Voltage measurements were performed using a Tektronix P6015A high-voltage probe with a shielded coaxial signal cable, and the probe grounding lead was kept as short as practicable to minimize parasitic inductance and transient interference.

To measure the transient current in the cable core of a submarine cable, a non-inductive sampling resistor with a nominal resistance of 0.2 Ω was connected in series in the grounding circuit at the end of the cable conductor. The current waveform was calculated based on the measured voltage across the sampling resistor and its nominal resistance. The accuracy of the calculated current amplitude was affected by the resistance value of the sampling resistor and the uncertainty in voltage measurement. Since the resistance of the sampling resistor

was much smaller than the wave impedance of the submarine cable itself, its interference with the overvoltage propagation process can be neglected.

To ensure measurement accuracy, the key equipment was calibrated prior to each test. Specifically, the wavefront and wavetail resistances of the impulse voltage generator were adjusted to ensure that the output waveform complies with the 1.2/50 μs lightning impulse parameters specified in the IEC 60060-1 standard; the measurement accuracy of the oscilloscope and high-voltage probe was calibrated; and a multimeter was used to verify the actual resistance value of the sampling resistor.

This experiment was primarily divided into two groups. In the first group, both the cable-core terminal and the metal sheath were left floating. A standard lightning impulse was applied to the cable's leading end, and high-voltage probes were used to measure the voltage at both the leading and trailing ends of the metal sheath. In the second group, the end of the cable core was grounded via a sampling resistor. Two test conditions were set up: one with the metal sheath suspended and the other with the end of the metal sheath grounded. A standard lightning impulse was applied to the cable's leading end, and measurements were taken of both the voltage across the metal sheath and the voltage drop across the sampling resistor.

All tests were conducted using standard positive-polarity, non-oscillating lightning impulse voltages, with a 5 min interval between consecutive impulses. During each interval, the cable specimen was discharged using a discharge rod to release residual free charges from the conductor and metallic sheath, thereby reducing their influence on subsequent measurements. Five repeated tests were conducted for each experimental configuration under the same conditions. The principal waveform characteristics, including peak polarity, temporal sequence, and oscillation trends, were consistent across the repeated tests, although some variations in peak amplitudes were observed. A representative waveform was selected from each group for presentation.

3. Analysis of Experimental Results

Based on the high-voltage impulse test platform described above, this section simulates the coupled operating conditions of the cable core and sheath under typical boundary conditions, measures and analyzes their transient response waveforms, and reveals the propagation patterns of overvoltage.

3.1. Capacitive Coupling

With both the cable core and the sheath fully suspended, a standard lightning impulse was applied to the leading end of the submarine cable. The voltage at the leading end of the cable core is shown in Figure 3, and the voltage across the metal sheath is shown in Figure 4.

As shown in Figure 3, the impulse voltage generator applies a standard lightning impulse voltage with an amplitude of 30.6 kV to the leading end of the cable core. Since the cable core is suspended, it can be approximated that the voltage across the entire length of the cable core is equal to the output voltage of the impulse voltage generator. As shown in Figure 4, the voltage waveforms and amplitudes at the leading and trailing ends of the sheath are nearly identical to those of the cable core. At this point, the sheath voltage relative to ground can be approximated as being caused by capacitive coupling of the cable-core voltage.

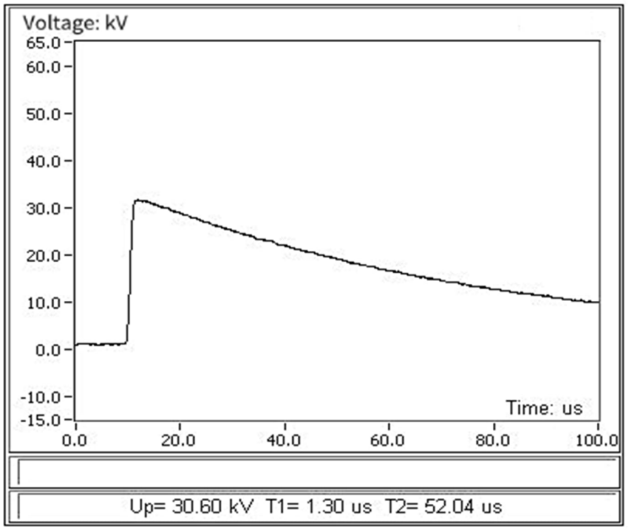


Figure 3. Injection voltage when the cable core and sheath are suspended.

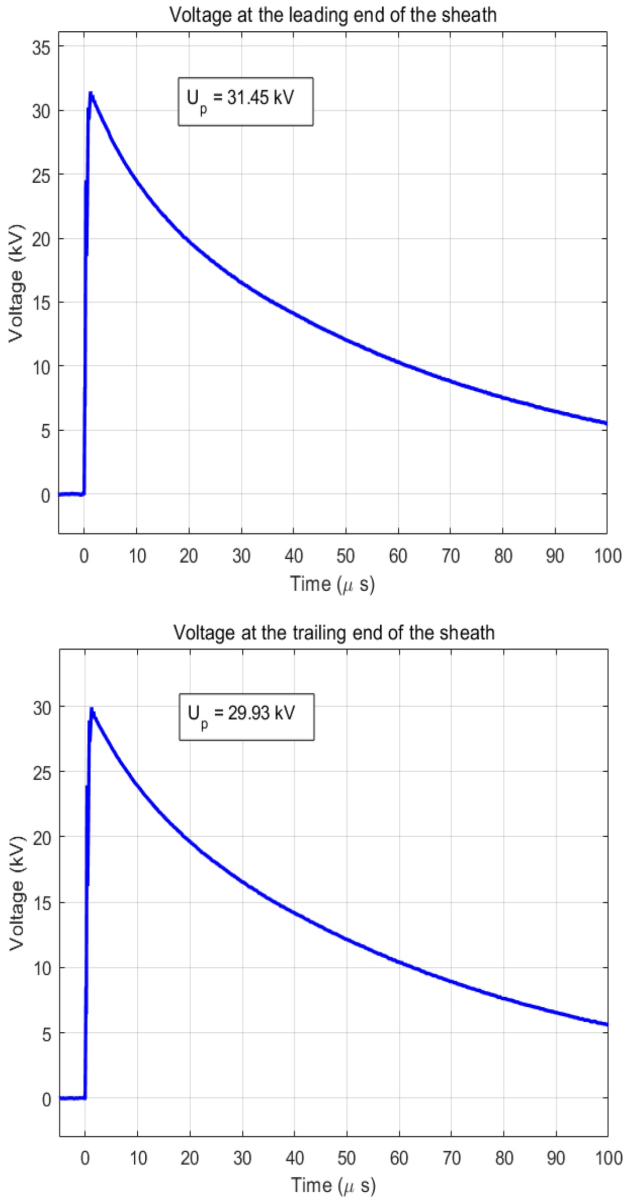


Figure 4. Sheath voltage when the cable core and sheath are suspended.

The structure of a submarine cable naturally forms a series-connected, two-stage coaxial capacitor. In this case, the sheath-to-ground voltage U_s strictly follows the voltage division relationship for capacitors:

$$U_s = U_c \cdot \frac{C_{12}}{C_{12} + C_{2g}} \quad (1)$$

where U_c, C_{12}, and C_{2g} represent, respectively, the peak value of the impulse voltage between the cable core and ground, the distributed capacitance per unit length between the cable core and the metal sheath, and the distributed capacitance per unit length between the metal sheath and ground.

Because the cable's primary insulation is thin and has a high relative permittivity—with C_{12} being much greater than C_{2g}—the peak voltage at the sheath is approximately equal to the core voltage. As can also be seen in Figure 4, the peak voltage at the trailing end of the sheath is slightly lower than the core voltage, while the peak voltage at the leading end of the sheath is slightly higher than the core voltage.

Figure 5 shows the voltage difference between the leading and trailing ends of the sheath when the cable core and sheath are suspended. Although no continuous current flows through the cable core under steady-state conditions, the charging current of the cable-core's distributed capacitance still generates a weak inductive coupling via mutual inductance during transient events. Since inductive coupling produces only a differential-mode potential difference in the axial direction of the sheath, this results in the voltage at the leading end of the sheath being slightly greater than the voltage at the cable core. However, at this point, the common-mode capacitive component is much greater than the differential-mode inductive component. Therefore, it can be approximated that only capacitive coupling effects are present in the sheath.

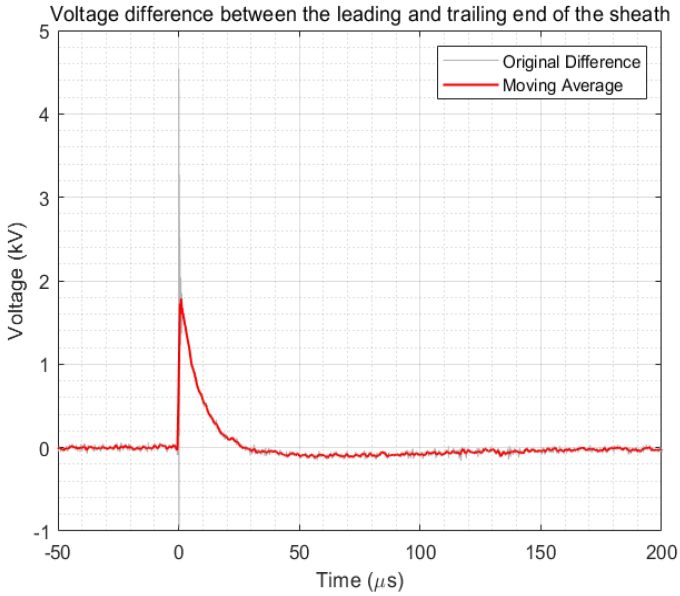


Figure 5. Voltage difference between the leading and trailing end of the sheath when the cable core and sheath are suspended.

After clarifying the characteristics of pure capacitive coupling in a fully suspended state, subsequent experiments introduced a grounded boundary to further investigate the suppression effect of ground loops in practical engineering applications and to observe the dominant role of inductive coupling.

3.2. Inductive Coupling

The end of the cable core was grounded via a sampling resistor, and the end of the metal sheath was grounded. A standard lightning impulse was applied to the leading end of the submarine cable. The voltage at the leading end of the cable core is shown in Figure 6. Because the cable core was directly grounded, the transient voltage was cut off before reaching its peak and rapidly dropped back to zero potential.

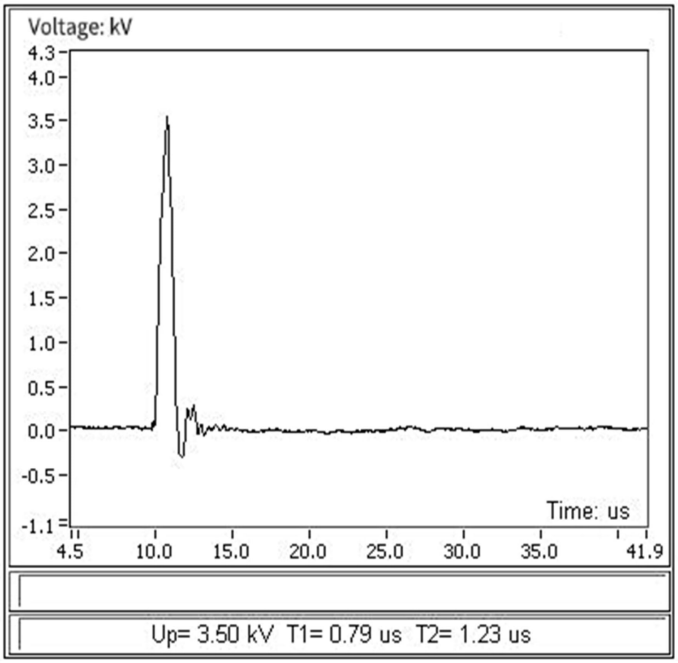


Figure 6. Injection voltage when the cable core and sheath are grounded.

Figure 7 shows the voltage at the leading end of the metal sheath when the trailing end of the metal sheath is grounded. The voltage waveform rises rapidly to a positive peak, then drops rapidly from the peak to 0 V, continues to decline from 0 V, reaches a negative peak, and finally rises slowly from the negative peak back to 0 V.

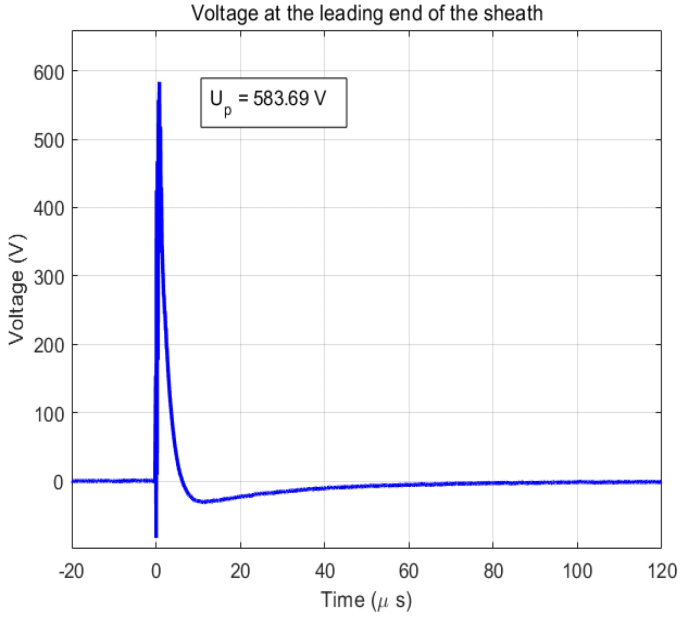


Figure 7. Voltage at the leading end of the metal sheath when the trailing end of the metal sheath is grounded.

The current in the cable core of the submarine cable is shown in Figure 8. When the sheath is grounded at its trailing end, the voltage at the leading end of the metal sheath can be approximated as being caused by inductive coupling. The physical mechanism of inductive coupling lies in the time-varying spatial magnetic field produced by transient variations in the cable-core current. This varying magnetic field induces eddy currents in the surrounding area, which in turn act on the free charges within the sheath, thereby generating an induced electromotive force.

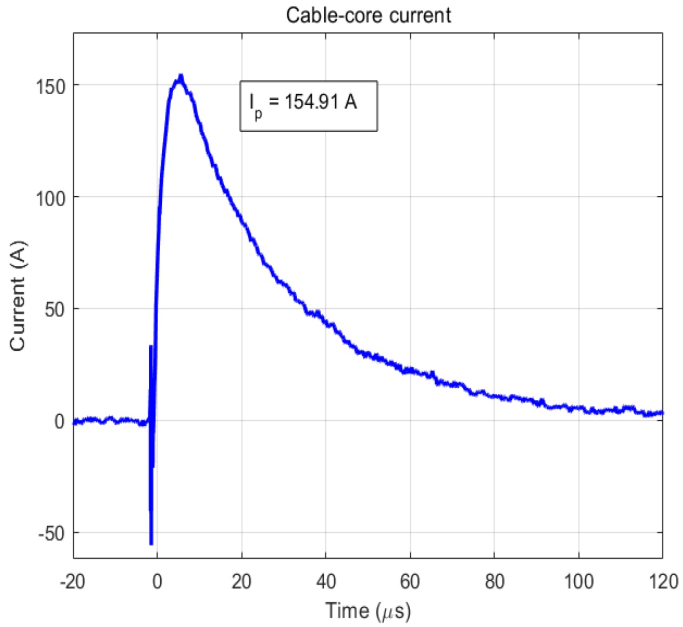


Figure 8. Cable-core current when the core and sheath are grounded.

The instantaneous value $e(t)$ of the induced electromotive force satisfies Faraday's law:

$$e(t) = -\frac{d\Psi}{dt} = -M \cdot \frac{di}{dt} \tag{2}$$

where the negative sign indicates that the direction of the induced electromotive force is opposite to that of the current in the cable core. The direction of the induced electromotive force can be determined using Lenz's law.

Figure 9 shows a comparison of the waveforms for the cable-core current and the sheath voltage. The current flowing from the cable head to the tail is defined as the positive direction. When the end of the sheath is grounded, the potential at point B is zero. Then the potential at point A is:

$$u_A(t) = \varphi_A(t) = M \cdot \frac{di}{dt} \tag{3}$$

The current in the cable core follows an impulse waveform—it rises rapidly to its peak and then descends slowly. The rate of change in the current is divided into two phases, and therefore the potential at point A also corresponds to two phases.

The first stage is the rising edge of the current. At the beginning of the rising edge, the current starts from zero and increases; at this point, the rate of change in the current is greater than zero and reaches its maximum positive value, so the potential at point A also rises rapidly from zero to its positive peak. As the current amplitude continues to increase, the rate of change in the current continues to decrease. When the current reaches its peak, the rate of change in the current is zero; therefore, during this process, the potential at point A continues to decrease from its highest positive value and returns to zero at the moment the current reaches its peak.

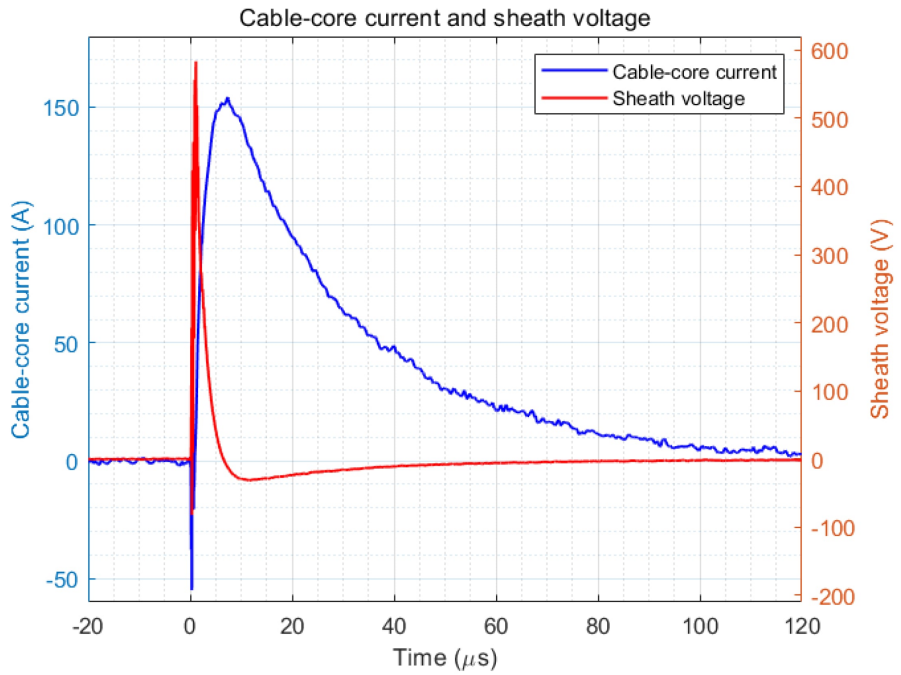


Figure 9. Cable-core current and sheath voltage.

The second stage is the falling edge of the current. At the beginning of the falling edge, the current is greater than zero but continues to decrease; at this point, the rate of change in the current is less than zero and reaches its maximum negative value, so the potential at point A also drops rapidly from zero to the negative peak. As the current amplitude continues to decrease, the absolute value of the rate of change in the current continues to decrease. When the current drops to zero, the rate of change in the current is zero; therefore, during this process, the potential at point A gradually rises from the negative peak and eventually returns to zero.

Figure 10 shows the induced voltage at the trailing end of the sheath when the leading end of the sheath is grounded. The potential at point A is zero. Therefore, the potential at point B is:

$$\varphi_B(t) = -M \cdot \frac{di}{dt} \tag{4}$$

Comparing Figure 10 with Figure 7, it can be seen that because the integration directions at the start and end points are opposite, the induced voltages measured at both ends exhibit mirror symmetry with respect to the zero-potential axis. The induced voltage at the leading end is slightly higher due to traveling-wave oscillations and weak capacitive coupling. The submarine cable used in this experiment was relatively short, and one end of its metal sheath was grounded. Under these experimental conditions, the low-impedance grounding path significantly suppressed the sheath-to-ground voltage caused by capacitive coupling. At the same time, the measured axial sheath voltage was primarily attributed to inductive coupling resulting from rapid changes in the conductor current. However, distributed capacitance between the conductor and the metal sheath still exists. Therefore, capacitive coupling is merely suppressed rather than eliminated.

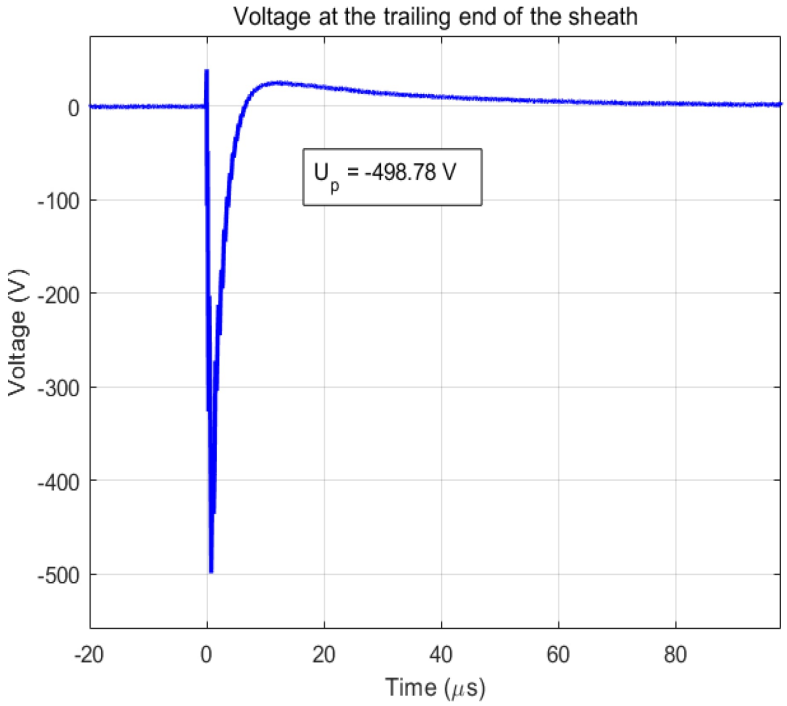


Figure 10. Voltage at the trailing end of the sheath when the cable core and the leading end of the sheath are grounded.

3.3. Superposition Coupling

The end of the cable core was grounded via a sampling resistor, with the metal sheath left floating. A standard lightning impulse was applied to the leading end of the submarine cable. The voltage at the leading end of the submarine cable core is shown in Figure 11.

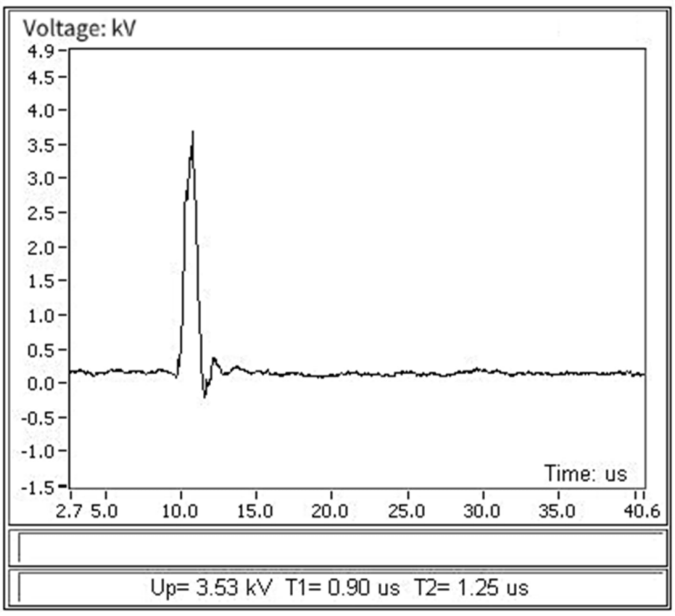


Figure 11. Injection voltage waveform with the cable core grounded and the sheath suspended.

The voltage at the leading and trailing ends of the sheath is shown in Figure 12. At this point, both capacitive coupling and inductive coupling are present on the sheath. The axial differential-mode electromotive force generated by inductive coupling is superimposed on the common-mode voltage generated by capacitive coupling. Comparative studies

indicate that the grounded condition eliminates the capacitive component, whereas the floating condition reveals the physical nature of the potential as a dynamic superposition of common-mode and differential-mode components.

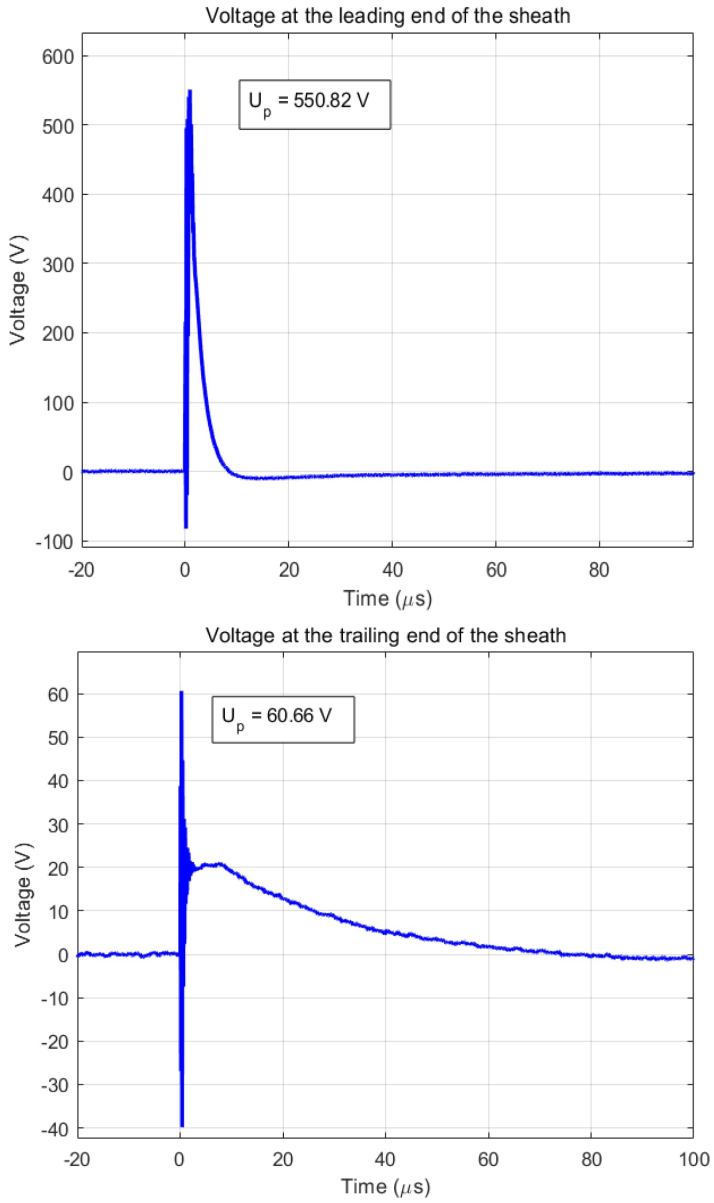


Figure 12. Sheath voltage when the cable core is grounded and the sheath is suspended.

Figure 13 presents the cable-core current under the condition that the cable core is grounded and the sheath is suspended. Figure 14 shows the voltage difference between the leading and trailing ends of the sheath under the same conditions. Comparing Figure 13 with Figure 8 reveals that the conductor current under different operating conditions is nearly identical. Similarly, comparing Figure 14 with Figure 7 reveals that the voltage difference between the leading and trailing ends of the sheath under different operating conditions is also nearly identical. This indicates that regardless of whether the metallic sheath is grounded or floating, the axial induced electromotive force difference across its ends is uniquely determined by the rate of change in the conductor's transient current, the mutual inductance coefficient, and the physical length of the cable.

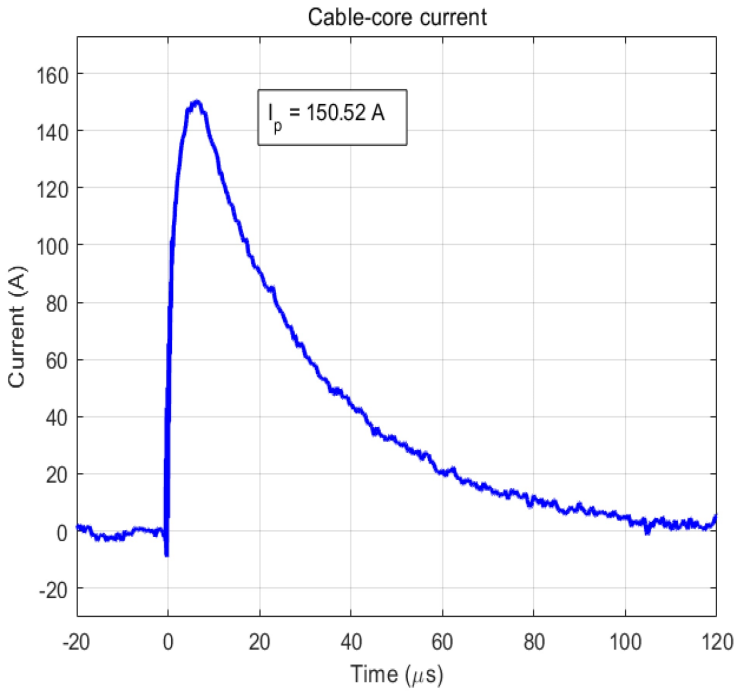


Figure 13. Cable-core current when the cable core is grounded and the sheath is suspended.

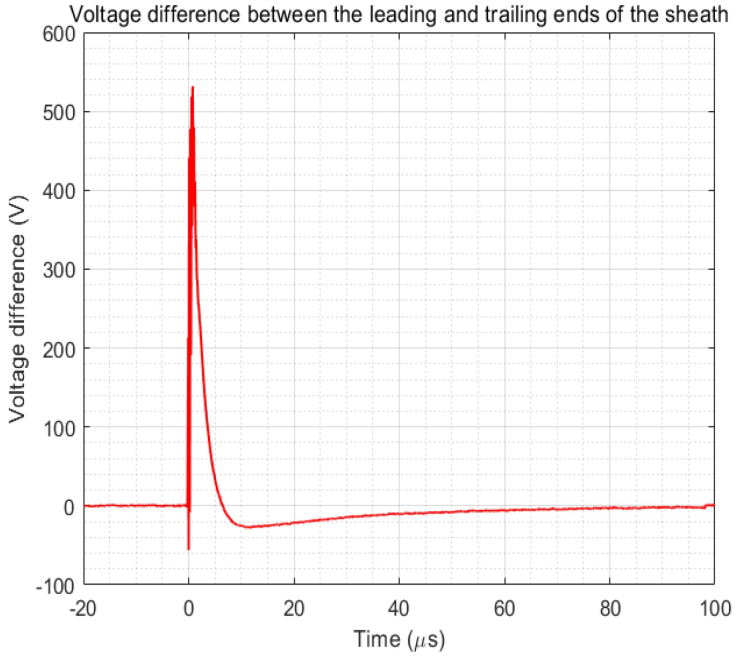


Figure 14. Voltage difference between the leading and trailing ends of the sheath when the cable core is grounded and the sheath is suspended.

4. Conclusions

Based on the above study of lightning impulse overvoltages in submarine cables, the following conclusions can be drawn:

(1) When both the conductor terminal and the metal sheath were in a suspended state, the measured sheath-to-ground voltage exhibited a trend that is essentially consistent with that of the impulse voltage applied to the conductor. This indicates that, under the suspended operating conditions studied, radial capacitive coupling is the primary mechanism determining the transient potential of the metal sheath.

(2) When the end of the conductor and one end of the metal sheath were grounded, the sheath-to-ground voltage caused by capacitive coupling was significantly suppressed. The transient potential difference along the axial direction of the sheath exhibited characteristics consistent with inductive coupling caused by rapid changes in the conductor current. This indicates that the grounding conditions of the metal sheath have a significant impact on the relative contributions of capacitive and inductive coupling.

(3) When the conductor's end was grounded and the metal sheath remained suspended, the measured sheath voltage exhibited characteristics resulting from the combined effects of capacitive and inductive coupling. Therefore, under the experimental conditions studied, the sheath potential could be understood as the superposition of the common-mode component generated by capacitive coupling and the axial induced potential difference generated by inductive coupling.

From an engineering perspective, these findings highlight the importance of appropriate metallic-sheath grounding and overvoltage protection arrangements. For single-point grounding configurations, the transient voltage at the ungrounded sheath end should be considered, and a suitably rated sheath voltage limiter may be required. For longer submarine cables, the electromagnetic induction model suggests that additional grounding points may help limit the accumulation of axial induced electromotive force by reducing the effective coupling length.

Author Contributions: Data curation, Y.H. and J.Z.; Funding acquisition, Y.H.; Investigation, Y.H. and J.Z.; Writing, Y.H. and J.Z.; Formal analysis, Y.H., W.L., J.Z., T.H. and Y.Z.; Methodology, Y.H., W.L., J.Z., T.H. and Y.Z. All authors have read and agreed to the published version of the manuscript.

Funding: This research was supported by the Science and Technology Project of State Grid Fujian Electric Power Co., Ltd. (Overvoltage mechanisms, monitoring strategies, and suppression techniques for long-distance HVDC submarine cable lines, No. 521304250013).

Data Availability Statement: The original contributions presented in this study are included in the article. Further inquiries can be directed to the corresponding author.

Conflicts of Interest: Authors Youcong Huang, Wenqi Li, and Junfeng Zhang were employed by the State Grid Fujian Electric Power Research Institute. The remaining authors declare that the research was conducted in the absence of any commercial or financial relationships that could be construed as a potential conflict of interest. The authors declare that this study received funding from State Grid Fujian Electric Power Co., Ltd. The funder was not involved in the study design, collection, analysis, interpretation of data, the writing of this article or the decision to submit it for publication.

References

1. Tumse, S.; Bilgili, M.; Yildirim, A.; Sahin, B. Comparative Analysis of Global Onshore and Offshore Wind Energy Characteristics and Potentials. *Sustainability* **2024**, *16*, 6614. [CrossRef]
2. Song, D.; Fan, T.; Li, Q.; Joo, Y.H. Advances in Offshore Wind. *JMSE* **2024**, *12*, 359. [CrossRef]
3. Su, X.; Wang, X.; Xu, W.; Yuan, L.; Xiong, C.; Chen, J. Offshore Wind Power: Progress of the Edge Tool, Which Can Promote Sustainable Energy Development. *Sustainability* **2024**, *16*, 7810. [CrossRef]
4. Yildirim, A.; Bilgili, M.; Tumse, S.; Sahin, B. Current and Future Trends of Offshore Wind Energy: A Comparative Analysis of World and Türkiye. *Mar. Georesources Geotechnol.* **2025**, *44*, 1138–1162. [CrossRef]
5. Guo, X.; Chen, X.; Chen, X.; Sherman, P.; Wen, J.; McElroy, M. Grid Integration Feasibility and Investment Planning of Offshore Wind Power under Carbon-Neutral Transition in China. *Nat. Commun.* **2023**, *14*, 2447. [CrossRef] [PubMed]
6. Yang, N.; Yang, J.; Pang, M.; Zhang, P.; Chang, Y.; Zhang, L.; Hao, Y.; Chen, Y. Decarbonization of the Wind Power Sector in China: Evolving Trend and Driving Factors. *Environ. Impact Assess. Rev.* **2023**, *103*, 107292. [CrossRef]
7. Deng, X.; Xu, W.; Xu, Y.; Shao, Y.; Wu, X.; Yuan, W.; Qin, Z. Offshore Wind Power in China: A Potential Solution to Electricity Transformation and Carbon Neutrality. *Fundam. Res.* **2024**, *4*, 1206–1215. [CrossRef] [PubMed]
8. Chen, Y.; Lin, H. Overview of the Development of Offshore Wind Power Generation in China. *Sustain. Energy Technol. Assess.* **2022**, *53*, 102766. [CrossRef]

9. Tu, Q.; Liu, Z.; Li, B.; Mo, J. Achieving Grid Parity of Offshore Wind Power in China—A Comparative Analysis among Different Provinces. *Comput. Ind. Eng.* **2021**, *162*, 107715. [CrossRef]
10. Wei, Y.; Zou, Q.-P.; Lin, X. Evolution of Price Policy for Offshore Wind Energy in China: Trilemma of Capacity, Price and Subsidy. *Renew. Sustain. Energy Rev.* **2021**, *136*, 110366. [CrossRef]
11. Satymov, R.; Bogdanov, D.; Breyer, C. Techno-Economics of Offshore Wind Power in Global Resolution. *Appl. Energy* **2025**, *393*, 125980. [CrossRef]
12. Li, R.; Jin, X.; Yang, P.; Liu, Y.; Wang, S.; Feng, Y.; Zheng, Y.; Cai, C.; Wang, L.; Xiao, K.; et al. Large-Scale Offshore Wind Integration by Wind-Thermal-Electrolysis-Battery (WTEB) Power System: A Case Study of Yangxi, China. *Int. J. Hydrogen Energy* **2024**, *52*, 467–484. [CrossRef]
13. Ou, C.; Chen, X.; Hu, K.; Cao, Y.; Shao, Y. Factors Influencing the Digital Intelligence Transformation of Offshore Wind Power Enterprise. *Ocean Coast. Manag.* **2024**, *259*, 107463. [CrossRef]
14. Liu, C.; Dong, B. China's Rapidly Expanding Offshore Wind Sector: Legal Risks and Regulatory Gaps in a Policy-Driven Industry. *Front. Mar. Sci.* **2026**, *13*, 1829508. [CrossRef]
15. Zhang, J.; Wang, H. Development of Offshore Wind Power and Foundation Technology for Offshore Wind Turbines in China. *Ocean Eng.* **2022**, *266*, 113256. [CrossRef]
16. Lu, B.; Li, S.; Cui, Y.; Zhao, X.; Zhang, D.; Kang, Y.; Dong, H. Insulation Degradation Mechanism and Diagnosis Methods of Offshore Wind Power Cables: An Overview. *Energies* **2022**, *16*, 322. [CrossRef]
17. Zhang, Y.; Wang, Y.; Zhang, D.; Zhang, W.; Wu, Z.; Hu, M. Effect of Seawater Corrosion on Aging Performance of Cross-Linked Polyethylene Cable Insulation. In *IEEE Transactions on Dielectrics and Electrical Insulation*; IEEE: New York, NY, USA, 2026.
18. Gulski, E.; Anders, G.J.; Jongen, R.A.; Parciak, J.; Siemiński, J.; Piesowicz, E.; Paszkiewicz, S.; Irska, I. Discussion of Electrical and Thermal Aspects of Offshore Wind Farms' Power Cables Reliability. *Renew. Sustain. Energy Rev.* **2021**, *151*, 111580. [CrossRef]
19. Wang, W.; Cheng, J.; Sun, Y.; Liu, J.; Shi, D.; Li, F. Effect of Seawater Immersion on Power Frequency Over Voltage Calculation of AC Three-Core Submarine Cable. *IOP Conf. Ser. Mater. Sci. Eng.* **2020**, *740*, 012094. [CrossRef]
20. Qian, M.; Zhao, D.; Chen, N.; Wang, Y.; Hu, Z. Characteristic Analysis of Overvoltage in Offshore Wind Power Transmission System through HVAC Submarine Cable. In *2021 IEEE Sustainable Power and Energy Conference (iSPEC)*; IEEE: New York, NY, USA, 2021; pp. 366–370.
21. Yaowei, X.; Xinlong, Z.; Binjie, C.; Zheng, X. Calculation of Transient Overvoltage in AC Submarine Cable System. *High Volt. Appar.* **2014**, *50*, 58–65.
22. Bak, C.L.; Faria da Silva, F. High Voltage AC Underground Cable Systems for Power Transmission—A Review of the Danish Experience, Part 1. *Electr. Power Syst. Res.* **2016**, *140*, 984–994. [CrossRef]
23. Mazzanti, G. HVDC Cable System Testing. *High Volt.* **2025**, *10*, 1349–1370. [CrossRef]
24. Liu, Y.; Yu, J.; Ma, M. Performance Evolution and Aging Mechanism of XLPE Insulation for HVDC Cables After Different Accelerated Aging. *IEEE Trans. Dielect. Electr. Insul.* **2025**, *32*, 1074–1083. [CrossRef]
25. Zou, L.; Han, S.; Han, Z.; Jia, R.; Liu, Q.; Liu, Z.; Ren, H. Thermal Pre-Aging-Dependent Seawater-Induced Degradation of XLPE Submarine Cable Insulation: Electrical Performance Evolution and Microstructural Mechanisms. *Polymers* **2026**, *18*, 1747. [CrossRef] [PubMed]
26. Tian, S.; Zhou, Y.; Liu, L.; Zhang, Y.; Zhao, H. Analysis of Resonance Mechanism of AC Submarine Cable Delivery System for Offshore Wind Power. *J. Phys. Conf. Ser.* **2024**, *2774*, 012093. [CrossRef]
27. Tharatak, P.; Jirapong, P.; Jan-ngoen, P. Analysis of Switching Transient Overvoltages and Protection Techniques for the Energization of the Connected 115 kV Underground and Submarine Cables. In Proceedings of the 2014 International Conference and Utility Exhibition on Green Energy for Sustainable Development (ICUE), Pattaya City, Thailand, 19–21 March 2014; pp. 1–6.
28. Benato, R.; Dambone Sessa, S.; De Zan, R.; Guarniere, M.R.; Lavecchia, G.; Sylos Labini, P. Different Bonding Types of Scilla–Villafranca (Sicily–Calabria) 43-Km Double-Circuit AC 380-kV Submarine–Land Cables. *IEEE Trans. Ind. Appl.* **2015**, *51*, 5050–5057. [CrossRef]
29. Vaideki, S.; Nivetha, M.; Jayaprakash; Pugazhendiran, P. Electric Field Analysis of High Voltage Submarine Cables. In *2017 International Conference on Computation of Power, Energy Information and Commuincation (ICCPEIC)*; IEEE: New York, NY, USA, 2017; pp. 778–782.
30. Gustavsen, B.; Sletbak, J. Transient Sheath Overvoltages in Armoured Power Cables. *IEEE Trans. Power Deliv.* **1996**, *11*, 1594–1600. [CrossRef]

Disclaimer/Publisher's Note: The statements, opinions and data contained in all publications are solely those of the individual author(s) and contributor(s) and not of MDPI and/or the editor(s). MDPI and/or the editor(s) disclaim responsibility for any injury to people or property resulting from any ideas, methods, instructions or products referred to in the content.